Dihydroartemisinin inhibits the activation and proliferation of hepatic stellate cells by regulating miR-29b-3p

SHENG HUAN[1-3], SUMIN SUN[3], SHILIAN SONG[1,2], JIN DAI[1,2], GUINING ZHU[1,2], YANLING ZHONG[1], YIHAO JI[2,4], SHIZHONG ZHENG[3] and GUOPING YIN[1]

[1]Department of Anesthesiology, The Second Hospital of Nanjing, Nanjing, Jiangsu 210037; [2]Nanjing Hospital Affiliated to Nanjing University of Chinese Medicine, Nanjing University of Chinese Medicine; [3]Jiangsu Key Laboratory for Pharmacology and Safety Evaluation of Chinese Materia Medica, Nanjing University of Chinese Medicine, Nanjing, Jiangsu 210046; [4]Department of Critical Medicine, Nanjing Second Hospital, Nanjing, Jiangsu 210037, P.R. China

Received March 11, 2022; Accepted June 22, 2022

DOI: 10.3892/ijmm.2023.5243

Abstract. Liver fibrosis is an early pathological feature of hepatic diseases. Hepatic stellate cell (HSC) activation and disordered proliferation are associated with liver fibrosis. The present study identified significant differences in the expression levels of microRNA (miRNA/miR)-29b-3p in clinical samples and multiple miRNA databases. Subsequently, the specific antifibrotic mechanism of miR-29b-3p was further elucidated. Reverse transcription-quantitative PCR, western blot, ELISA and immunofluorescence were used to detect the expression levels of target genes and proteins. Oil red O, Nile red and trypan blue staining were used to evaluate HSC activation and cell viability. A luciferase assay was used to detect the relationship between miR-29b-3p and VEGFA. Adhesion, wound healing, apoptosis double staining and JC-1 assays were used to detect the effects of VEGFR1 and VEGFR2 knockdown on HSCs. Immunoprecipitation and fluorescence colocalization were used to identify interactions between the proteins. Furthermore, a rat fibrosis model was constructed to investigate the effects of dihydroartemisinin (DHA) and miR-29b-3p *in vivo* and *in vitro*. The results indicated that miR-29b-3p both inhibited the activation of HSCs and limited the proliferation of activated HSCs via lipid droplet recovery and VEGF pathway regulation. VEGFA was identified as a direct target of miR-29b-3p, and knockdown of VEGFA induced cell apoptosis and autophagy. Notably, VEGFR1 and VEGFR2 knockdown both promoted apoptosis; however, VEGFR1 knockdown inhibited autophagy, whereas VEGFR2 knockdown induced autophagy. Furthermore, it was revealed that VEGFR2 regulated autophagy by mediating the PI3K/AKT/mTOR/ULK1 pathway. VEGFR2 knockdown also led to ubiquitination of heat shock protein 60, ultimately inducing mitochondrial apoptosis. Finally, DHA was identified as a natural agonist of miR-29-3p that effectively prevented liver fibrosis *in vivo* and *in vitro*. Overall, the present study determined the molecular mechanism by which DHA inhibited HSC activation and prevented liver fibrosis.

Correspondence to: Dr Guoping Yin, Department of Anesthesiology, The Second Hospital of Nanjing, 1-1 Zhongfu Road, Nanjing, Jiangsu 210037, P.R. China
E-mail: yinguoping0304@hotmail.com

Key words: dihydroartemisinin, hepatic stellate cells, microRNA-29b-3p, VEGFR2, molecular mechanism

Introduction

Liver fibrosis is the pathological basis of most liver diseases. Activation of static hepatic stellate cells (HSCs) and disordered proliferation are the main developmental steps of liver fibrosis (1-3). Drug toxicity, viral infection or alcohol may cause static HSCs to lose intracellular lipid droplets, release large amounts of extracellular matrix components, including α-SMA and COL1A1, and transform from a non-split phenotype to a myofibroblast-like cell phenotype (4,5). In other words, HSCs switch from an inactive state to an active state. Further exploration of the potential mechanism of HSCs development is required to prevent liver fibrosis.

Previous studies have reported the pivotal role of noncoding RNAs [including microRNAs (miRNAs/miRs), circular RNAs and long noncoding RNAs] in HSCs (6,7). miRNAs are a highly conserved form of noncoding single-stranded RNA, which consist of 20-26 bases, and regulate a variety of physiological and pathological processes in the body (8,9). miR-29b-3p has been reported to serve a key role in a wide range of pathological processes, such as myocardial injury, ion channel opening and insulin resistance (10,11). Although its antifibrotic function has been reported previously, the specific downstream mechanism has not been completely clarified.

VEGFA is secreted by hepatocytes and HSCs, and is the core factor for maintaining fenestration of hepatic sinusoidal endothelial cells; however, the specific crosstalk of VEGFA in the progression of hepatic fibrosis is unclear. VEGF has been reported to induce the transformation of HSCs into fibroblasts that proliferate and synthesize type I collagen in a rat model of liver fibrosis (12). Moreover, VEGF expression in HSCs has been shown to be significantly increased in hypoxic environments (13). Treatment of HSCs with recombinant VEGF

and recombinant angiopoietin-1 (Ang-1) can produce similar effects that transform HSCs into fibroblasts, and contribute to the proliferation and synthesis of type I collagen (12).

Autophagy is a ubiquitous phenomenon in eukaryotic cells that has an important role in numerous aspects of life. Autophagy is mainly mediated by the PI3K/AKT/mTOR, sirtuin (SIRT) and AMP-activated protein kinase (AMPK) pathways. The PI3K/AKT/mTOR pathway can negatively regulate autophagy-related protein activity, and PI3K agonists effectively block autophagy (1-3). Heat shock protein 60 (HSP60) is mainly distributed in the cytoplasm and mitochondria, and is encoded by the nuclear genome. Notably, HSP60 is important in the transport, activation and folding of mitochondrial proteins; therefore, imbalance of the HSP60 protein may induce mitochondrial destruction and apoptosis via the mitochondrial pathway (14).

Dihydroartemisinin (DHA) is a natural and safe antimalarial drug (15). Our previous studies confirmed that DHA protected rats from liver fibrosis induced by intraperitoneal injection of carbon tetrachloride (CCl_4) or bile duct ligation by influencing HSCs migration, contraction and senescence (16,17). However, to the best of our knowledge, the potential relationship between DHA and miR-29b-3p, and their specific downstream signals, have not been determined; the present study aimed to address this.

Materials and methods

Reagents and antibodies. DHA (cat. no. D7439), CCl_4 (cat. no. 488488) and dimethyl sulfoxide (cat. no. D2650) were purchased from MilliporeSigma. 740Y-P (cat. no. P0175) was purchased from MedChemExpress. Dulbecco's modified Eagle's medium (DMEM; cat. no. 11995-065), fetal bovine serum (FBS), phosphate-buffered saline (PBS), penicillin-streptomycin solution (100X), mitomycin and trypsin EDTA were purchased from Gibco, Thermo Fisher Scientific, Inc. Small interfering RNA (siRNA) targeting VEGFA, VEGFR1 and VEGFR2, and negative control (NC) siRNA were obtained by Nanjing KeyGen Biotech. Co., Ltd. Wild-type (WT) 3'UTR-psiCHECK2-VEGFA and mutant (MUT) 3'UTR-psiCHECK2-VEGFA plasmids were obtained by Hedgehogbio Co., Ltd. P3*Flag-CMV-14-HSP60 and its NC (empty plasmid) were purchased from Eproll. Co., Ltd. AAV8-GP-3-rno-miR-29b-3p mimic, AAV8-GP-3-rno-miR-29b-3p mimic NC, miR-29b-3p mimic, mir-29b-3p inhibitor and their NC vectors were obtained by Jima Biological Company. The corresponding siRNA and plasmid sequences are listed in Table SI.

Animal experiment. The animal experiment was approved by Institutional and Local Committee of Nanjing University of Chinese Medicine (approval no. A20402; Nanjing, China). The present study was carried out based on the guidelines of the Care and Use of Animals of Nanjing University of Chinese Medicine. A total of 36 male Sprague Dawley rats (weight, 220-260 g; age, 6 weeks) were purchased from Shanghai SLAC Laboratory Animal Co., Ltd. Rats were maintained under a standard 12-h light/dark cycle, at an indoor temperature of 20±2˚C and humidity of 50±10%, and their bedding was autoclaved. Rats received standard food (5 g/100 g/day) and drinking water (11 ml/100 g/day). The health and behavior of the animals were monitored once a day to ensure reliability of the experiments. A liver fibrosis model was constructed via intraperitoneal (IP) injection of CCl_4 and olive oil [1:9 (v/v); 0.5 ml/100 g body weight]. A total of 36 rats were randomly divided into the following six groups (6 rats/group): i) Control group, ii) CCl_4 group, iii) CCl_4 + AAV8-miR NC group, iv) CCl_4 + DHA group, v) CCl_4 + AAV8-miR group and vi) CCl_4 + AAV8-miR + DHA group. The dosage of DHA and administration route were selected based on our previous study (13). CCl_4 and olive oil were injected into rats in all of the groups, with the exception of the control group, every other day from week 1 to week 8. Rats in the control group received olive oil without CCl_4. At the beginning of week 4, rats in the CCl_4 + AAV8-miR NC group were administered AAV8-GP-3-rno-miR-29b-3p mimics NC ($6.02x10^{11}$ V.G/ml; 32 μl/100 g body weight), whereas rats in the CCl_4 + AAV8-miR and the CCl_4 + AAV8-miR + DHA group were administered AAV8-GP-3-rno-miR-29b-3p mimics ($4.16x10^{12}$ V.G/ml; 160 μl/100 g body weight) by caudal vein. At the beginning of week 2, rats in the CCl_4 + DHA group and the CCl_4 + AAV8-miR + DHA group were administered DHA by IP injection (3 mg/ml; 2 g/100 g body weight). DHA was suspended in olive oil and given once a day. The duration of the experiment was 2 months, starting from the first IP injection of CCl_4 until the end of the 8th week. After the experiment, the mice were weighed and were anesthetized with pentobarbital sodium (50 mg/kg). Blood was collected from the orbital vein of rats at a volume of 0.5 ml quickly without delay and immediately underwent biochemical index detection. Subsequently, the rats were euthanized by intraperitoneal injection of an overdose of pentobarbital sodium (100-150 mg/kg). Euthanasia was confirmed through the observation of respiratory, heartbeat, pupil and nerve reflexes, and other indications. Blood and liver samples were collected from rats in each group for serum biochemical analysis, tissue immunofluorescence, reverse transcription-quantitative PCR (RT-qPCR) and western blot analysis.

Hematoxylin and eosin (H&E), Masson's trichrome and Sirius Red staining. The rat liver tissues were fixed with 4% paraformaldehyde at 37˚C for 0.5 h. The liver tissues were then dehydrated with various concentrations of alcohol, embedded in paraffin and sectioned (5 μm). Subsequently, the sections were stained with hematoxylin (cat. no. BP-DL019; Nanjing SenBeiJia Biological Technology Co., Ltd.) for 5 min, washed with 1X PBS and differentiated with 1% hydrochloric alcohol for a few seconds at room temperature. Finally, the sections were stained with eosin (cat. no. BP-DL010; Nanjing SenBeiJia Biological Technology Co., Ltd.) for 3 min at room temperature. Masson's trichrome and Sirius red staining were used for the evaluation of collagen expression. The Masson's trichrome kit (cat. no. BP-DL371; Nanjing SenBeiJia Biological Technology Co., Ltd) and the Sirius red staining kit (cat. no. BP-DL030; Nanjing SenBeiJia Biological Technology Co., Ltd.) were carried out according to the manufacturer's instructions at room temperature. The representative images were obtained under an inverted light microscope (Zeiss GmbH).

Cell culture. HSCs-LX-2 cells (BNCC337957) were purchased from BeNa Culture Collection; Beijing Beina Chuanglian Institute of Biotechnology. The cells were cultured in DMEM containing 10% FBS and 1% penicillin-streptomycin solution (100X) at 37˚C in a humidified incubator with 5% CO_2 and 95% air.

Drug intervention. After the HSCs were cultured until they adhered to the wells, DHA was added at 10, 20 and 40 μM for 24 h at 37˚C. In addition, cells were treated with 740Y-P (15 μM) for 24 h at 37˚C, and with the VEGFR1-specific inhibitor GNQWFI or the VEGFR2-specific inhibitor SU5416 (0.02, 0.2, 2 and 10 μM) for 24 h at 37˚C.

Cell transfection. According to the instructions, 100 nM siRNA-VEGFA, miR-29b-3p mimic, miR-29b-3p inhibitor, siRNA-VEGFR1 and siRNA-VEGFR2, and 500 ng/μl CMV-14-HSP60, as well as their NCs (with the same concentration) were transfected into LX-2 cells ($3x10^5$ cells/well) in 6-well microplates with 3 μl Lipofectamine® 2000 (cat. no. 11668027; Thermo Fisher Scientific, Inc.). The ratio of plasmid or siRNA with Lipofectamine 2000 was 1:1. The transfected cells were cultured in normal conditions at 37˚C for 12 h. RT-qPCR was then performed to verify the transfection efficiency and subsequent experiments were performed. Subsequent experimentation was performed after 12 h of transfection.

RT-qPCR. The LX-2 cells were lysed with TRIzol® (Invitrogen; Thermo Fisher Scientific, Inc.), total RNA was collected with isopropanol (Shanghai Aladdin Biochemical Technology Co., Ltd.) and RNA content was determined using an enzyme labeling instrument. In addition, rat liver tissues were cut into pieces and rapidly frozen with liquid nitrogen prior to extraction of total RNA using TRIzol. RNA was then reverse transcribed into cDNA with Hifair® II 1st Strand cDNA Synthesis kit (Shanghai Yeasen Biotechnology Co., Ltd.) according to the manufacturer's protocol. cDNA was amplified with Hieff Qreal-time PCR SYBR Green main mixture (low Rox +) (Shanghai Yeasen Biotechnology Co., Ltd.) and detected using an Applied Biosystems 7500 system (Applied Biosystems; Thermo Fisher Scientific, Inc.) according to the manufacturer's instructions. qPCR was performed under the following conditions: Initial denaturation at 95˚C for 5 min, followed by 40 cycles at 95˚C for 15 sec, 60˚C for 60 sec and 72˚C for 40 sec, and a final step at 72˚C for 5 min. The expression levels of mRNA and miRNA were normalized to β-actin and U6 expression, respectively, and the $2^{-\Delta\Delta Cq}$ method was used to calculate the expression levels (13). The primer sequences used for RT-qPCR are listed in Table SI.

Western blot analysis. The LX-2 cells were washed with 1X PBS for three times and then total proteins were extracted using RIPA lysis buffer (cat. no. P0013C; Beyotime Institute of Biotechnology). The rat liver tissues was cut into pieces and rapidly frozen with liquid nitrogen prior to total protein extraction using RIPA lysis buffer. Total protein concentration was determined using the BCA protein analysis kit (cat. no. 23225; Thermo Fisher Scientific, Inc.). The same concentration of proteins (30 μg/sample) were separated by SDS-PAGE and the SDS gel percentage was chosen according to the molecular level of the target protein (10, 12 or 15%). Proteins were then transferred to PVDF membranes (microporous; cat. no. IPVH00010; MilliporeSigma) and blocked with 5% BSA (cat. no. ST025; Beyotime Institute of Biotechnology) at 37˚C for 1 h in TBS + 0.1% Tween-20. The PVDF membranes were then incubated with primary antibodies (1:1,000) at 4˚C overnight and with the secondary antibody (1:10,000) at 37˚C for 2 h. Finally, the membranes were incubated with ECL (cat. no. 32109; Thermo Fisher Scientific, Inc.) and band intensity was semi-quantified by Image Lab software v3.0 (Bio-Rad Laboratories, Inc.). The primary antibodies β-actin (cat. no. AF7018) were purchased from Affinity Biosciences Ltd. The primary antibodies against α-SMA (cat. no. 14395-1-AP), COL1A1 (cat. no. 67288-1-Ig), VEGFA (cat. no. 19003-1-AP) and VEGFR2 (cat. no. 26415-1-AP) were purchased from ProteinTech Group, Inc. The primary antibody against ubiquitin (cat. no. R26024) was purchased from Chengdu Zen Bioscience Co., Ltd. The primary antibodies against VEGFR1 (cat. no. A19132), AKT (cat. no. A20799), phosphorylated (p)-AKT (cat. no. AP1259), mTOR (cat. no. A2445), p-mTOR (cat. no. AP0115), ULK1 (cat. no. A8529), p-ULK1 (cat. no. AP0736), caspase-9 (cat. no. A18676), cytochrome *c* (cat. no. A4912), AIF (cat. no. A19536), LC3B (cat. no. A19665), Beclin-1 (cat. no. A7353) and P62 (cat. no. A19700) were purchased from ABclonal Biotech Co., Ltd. The HRP Goat Anti-Rabbit IgG (H+L) secondary antibody (cat. no. AS014) and HRP Goat Anti-Mouse IgG (H+L) secondary antibody (cat. no. AS003) were purchased from ABclonal Biotech Co., Ltd.

Immunofluorescence staining. The protein expression levels of LX-2 cells were measured by immunofluorescence staining. LX-2 cells ($1x10^5$ cells/well) were seeded into a 24-well microplate. After intervention, the cells were fixed with 4% paraformaldehyde at 37˚C for 0.5 h and blocked with 1% BSA at 37˚C for 2 h. The cells were incubated with primary antibodies against α-SMA (cat. no. 14395-1-AP), COL1A1 (cat. no. 67288-1-Ig) and VEGFA (cat. no. 19003-1-AP) (all from ProteinTech Group, Inc.) at 4˚C overnight (1:200) and with FITC-conjugated anti-rabbit or anti-mouse secondary antibodies (1:200; cat. nos. ab6717 and ab6785; Abcam) at 37˚C for 2 h. All images were captured under an inverted fluorescence microscope (Zeiss GmbH). Liver tissues (5 μm) were also assessed by immunofluorescence staining using the same technique as aforementioned.

Oil red O staining. LX-2 cells ($1x10^5$ cells/well) were seeded into 24-well microplates and stained with 200 μl oil red O (Nanjing Jiancheng Bioengineering Institute) at room temperature for 8 min according to the manufacturer's instructions. The representative images were obtained under an inverted light microscope (Zeiss GmbH).

Nile red staining. LX-2 cells ($1x10^5$ cells/well) were seeded into 24-well microplates and fixed with 4% paraformaldehyde at 37˚C for 0.5 h. Subsequently, they were stained with 500 μl Nile Red (Nanjing Jiancheng Bioengineering Institute) at 37˚C for 10 min according to the manufacturer's instructions. The representative images were obtained under an inverted light microscope (Zeiss GmbH).

Determination of triglyceride (TG) levels. The TG levels were measured using the TG detection kit (cat. no. SY6206; Yita Biological Co., Ltd.) according to the manufacturer's instructions. After transfection with miR-29b-3p mimic NC, miR-29b-3p mimic, miR-29b-3p inhibitor NC and miR-29b-3p inhibitor, the optical density of cells from the four aforementioned groups was determined at 570 nm using a plate reader (Thermo Fisher Scientific, Inc.).

Determination of cholesterol levels. The total cholesterol (TC) levels were measured using the TC detection kit (cat. no. SY6226; Yita Biological Co., Ltd.) according to the manufacturer's instructions. After transfection with miR-29b-3p mimic NC, miR-29b-3p mimic, miR-29b-3p inhibitor NC and miR-29b-3p inhibitor, the optical density of cells from the four aforementioned groups was determined at 570 nm using a plate reader (Thermo Fisher Scientific, Inc.).

IL-6 detection. IL-6 levels were measured using an IL-6 ELISA kit (cat. no. RK00004; ABclonal Biotech Co., Ltd.) according to the manufacturer's instructions. LX-2 cells ($3x10^4$ cells/well) were seeded into 96-well microplates and incubated at 37˚C for 24 h in 5% CO_2. After transfection with VEGFA siRNA, VEGFR1 siRNA and VEGFR2 siRNA, the optical density of the corresponding samples was determined at 570 nm using a plate reader (Thermo Fisher Scientific, Inc.).

Luciferase assay. LX-2 cells ($3x10^5$ cells/well) were seeded into a 6-well microplate. Subsequently, 100 nM miR-29b-3p mimic NC or 100 nM miR-29b-3p mimic was transfected into LX-2 cells, and then 200 ng WT 3'UTR-psiCHECK2-VEGFA vector or MUT 3'UTR-psiCHECK2-VEGFA vector (cat. no. HH-LUC-036, HedgehoBio Science and Technology Co., Ltd.) was transfected into cells with Lipofectamine 2000 at 37˚C for 12 h in an atmosphere containing 5% CO_2. Subsequently, cells ($1.0x10^5$ cells/ml) were lysed with the lysis buffer in the Luciferase Reporter Gene Assay Kit (cat. no. 11401ES60; Shanghai Yeasen Biotechnology Co., Ltd.), collected and treated with luciferase test reagent (cat. no. 11401-B; Shanghai Yeasen Biotechnology Co., Ltd.). Luciferase activity was measured using a Multiskan FC photometer (Thermo Fisher Scientific, Inc.). Luciferase activity was normalized to a blank control group.

Mitochondrial membrane potential detection. LX-2 cells ($1x10^5$ cells/well) were seeded into 24-well microplates and incubated for 24 h at 37˚C in 5% CO_2. After intervention, the LX-2 cells were treated with 10 μM JC-1 reagent (cat. no. SY0910; Yita Biological Co., Ltd.) at 37˚C for 15 min. Subsequently, JC-1 aggregate fluorescence (excitation wavelength, 530 nm; emission wavelength, 583 nm) and JC-1 monomer fluorescence (excitation wavelength, 488 nm; emission wavelength, 525 nm) were measured using a Multiskan FC photometer (Thermo Fisher Scientific, Inc.). Representative images were captured using an inverted fluorescence microscope (Zeiss GmbH).

Annexin V-FITC/PI double staining. Annexin V-FITC/PI double staining assay was conducted with the Annexin V-FITC Apoptosis Detection Kit (Beyotime Institute of Biotechnology). LX-2 cells were collected and dissolved in Annexin V-FITC binding buffer at a density of $1.0x10^6$ cells/ml. Subsequently, 100 μl sample solution was treated with 5 μl FITC-conjugated Annexin V reagent and 5 μl PI reagent, and incubated at room temperature for 15 min in the dark. The percentages of cells within each quadrant (Q1, Q3, Q3 and Q4) were determined using a Gallios flow cytometer (Beckman Coulter, Inc.). The results were analyzed by FlowJo software v10.6.2 (FlowJo, LLC).

Immunoprecipitation assay. LX-2 cells were washed with 1X PBS and total proteins were extracted using 500 μl RIPA lysis buffer (Beyotime Institute of Biotechnology). The homogenates were centrifuged at 1,300 x g for 30 min at 4˚C. Subsequently, 20% of the lysate supernatant was used as the input for western blot analysis and the remaining lysate was used to perform the immunoprecipitation assay. The binding/detergent solution (20 mM Na_2HPO_4, 0.15 M NaCl; pH 7.0) was prepared for later use. The HSP60 antibody (cat. no. A0564) was purchased from ABclonal Biotech Co., Ltd.; 5 μl HSP60 antibody was added to the remaining lysate, and the proteins were shaken overnight at 4˚C. Subsequently, 50 μl protein A/G plus agarose beads (Santa Cruz Biotechnology, Inc.) were added to the previously prepared antigen-antibody binding complex at 4˚C overnight to make them couple with each other. Subsequently, the bead-antibody-antigen complex was centrifuged at 1,300 x g for 3 min at 4˚C. The supernatant was carefully extracted, and the agarose beads were washed with 1 ml binding/detergent solution three times. After washing, the magnetic bead-antibody-antigen complex was added to 30 μl 2X SDS-PAGE loading buffer, mixed and heated in a 95˚C water bath for 15 min. The supernatant was then taken for western blot analysis.

Cell Counting Kit-8 (CCK-8) assay. LX-2 cells ($3x10^4$ cells/well) were seeded into 96-well microplates and incubated at 37˚C for 24 h in 5% CO_2. After intervention, cells were treated with 10 μl CCK-8 reagent (Shanghai Yeasen Biotechnology Co., Ltd.) and incubated at 37˚C for 4 h. The optical density was determined at 570 nm using a plate reader (Thermo Fisher Scientific, Inc.).

Trypan blue staining. LX-2 cells ($1x10^5$ cells/well) were seeded into 24-well microplates and incubated at 37˚C for 24 h in 5% CO_2. After intervention, the cells were treated with 0.4% trypan blue solution (MilliporeSigma) at a ratio of 9:1 at room temperature for 3 min. The representative images were obtained under an inverted light microscope (Zeiss GmbH).

Adhesion assay. Rat tail tendon collagen type I (cat. no. C8062; Beijing Solarbio Science & Technology Co., Ltd.) was used to coat a 96-well microplate at the concentration of 2 mg/ml, which was dissolved in 0.006 mol/l acetic acid. NaOH (0.1 mol/l) was then added to promote gelation at 37˚C for 2 h. The uncoated well was used as the negative control. Each well was washed three times with 1X PBS, and the LX-2 cells ($5x10^4$ cells/well) were seeded into the coated and uncoated wells, before being incubated for 0.5, 1 and 2 h at 37˚C in 5% CO_2. Subsequently, each well was washed with 1X PBS to remove the unattached cells. The viability of adherent cells was measured using an

MTT assay. Dimethyl sulfoxide was used to dissolve the purple formazan and the absorbance values at 490 nm were measured using a Synergy2 Microplate reader (BioTek Corporation). The representative images at 2 h were obtained under an inverted light microscope (Zeiss GmbH).

Wound healing assay. LX-2 cells ($3x10^5$ cells/well) were seeded into a 6-well microplate until they formed a 90% confluent monolayer. The tip of a 200-μl sterile pipette was used to generate an artificial and uniform wound, and the unattached cells were carefully removed with 1X PBS. Cells were firstly treated with mitomycin at the concentration of 1 μg/ml at 37˚C for 1 h in 5% CO_2 to inhibit cell division and then incubated in serum-free medium at 37˚C for 12 h in 5% CO_2. The representative images at 0 and 12 h were captured under an inverted light microscope (Zeiss GmbH). The horizontal distance of the wound was calculated with ImageJ v1.8.0 (National Institutes of Health).

Molecular docking prediction. AutoDock Vina molecular docking software was used to simulate the combination of DHA and VEGFA proteins (http://autodock.scripps.edu/resources/raccoon) (18).

Serum biochemistry. Blood was collected into clot activating tubes from rat orbital veins and was then centrifuged at 300 x g for 15 min at room temperature to collect the supernatant. An automatic biochemical analyzer (Hitachi, Ltd.) was used to detect the concentration of liver injury-related indicators alanine aminotransferase (ALT), aspartate aminotransferase (AST) and alkaline phosphatase (ALP), as well as the liver fibrosis-related indicators hyaluronic acid (HA), laminin (LN), type III procollagen (PC-III) and type IV collagen (IV-C) in rat serum.

Datasets. The enrichment analysis of differentially expressed genes was conducted using bioinformatics analysis and Kyoto Encyclopedia of Genes and Genomes (KEGG). The liver fibrosis-related miRNAs were analyzed using the following databases: GSE33857 (19), GSE49012 (20), GSE59492 (21), GSE74872 (22) from Gene Expression Omnibus (GEO) (http://www.ncbi.nih.gov/geo) (23), miRWalk (http://mirwalk.umm.uni-heidelberg.de/) (24), miR2Disease (http://www.mir2disease.org/) (25) and HMDD (http://www.cuilab.cn/hmdd) (26). The potential interactions between VEGFA and HSP60 protein were predicted using the following database: GeneMania (http://www.genemania.org/) (27). The target genes of miR-29b-3p were predicted using the following databases: miRWalk (http://mirwalk.umm.uni-heidelberg.de/), miRND (http://mirdb.org/) and TargetScan (https://www.targetscan.org/) (28). The thresholds in the GEO database were set as follows: P<0.05, fold change of all and gene rank of all. The KEGG enrichment analysis of differentially expressed genes between patients with different stages of liver fibrosis in the GSE33258 GEO dataset was performed using the ASSISTANT for Clinical Bioinformatics (https://www.aclbi.com/) (29). For KEGG analysis, P<0.05 or FDR <0.05 was considered to be a meaningful pathway [enrichment score with -log10(P) >1.3].

Statistical analysis. The present data are presented as the mean ± standard deviation. GraphPad Prism 7.0 was used to analyze the significance of the results (GraphPad Software, Inc.). Statistical significance was determined using an unpaired Student's t-test for comparisons between two groups, or one-way ANOVA followed by Tukey's post hoc test for comparisons among more than two groups. P<0.05 was considered to indicate a statistically significant difference. Each experiment was repeated at least three times.

Results

miR-29b-3p upregulation inhibits HSC development in vitro. Our previous study revealed that lncRNA H19 can prevent liver fibrosis *in vivo* and *in vitro* (30). The present study aimed to screen liver fibrosis-related miRNAs and explore their underlying mechanisms. Between normal and hepatic fibrosis samples, five significantly differentially expressed miRNAs were identified in four GEO datasets (GSE33857, GSE49012, GSE59492 and GSE74827), and two differentially expressed miRNAs were identified in three public databases (miRWalk, miR2Disease and HMDD) (Fig. 1A). Only miR-29b was revealed to be differentially expressed in all databases. Since miR-29b has two subtypes miR-29b-1 and miR-29b-2, and their 3p-ends are the same but their 5p-ends are different, miR-29b-3p was selected for further analysis (Fig. 1A).

The transfection efficacy of the miR-29b-3p mimic and miR-29b-3p inhibitor was confirmed by RT-qPCR (Fig. 1B). Notably, transfection with the miR-29b-3p mimic decreased the mRNA and protein expression levels of the fibrotic markers α-SMA and COL1A1 in LX-2 cells, whereas the inhibitor increased them (Figs. 1C, D and S1A). A previous study confirmed that COL1A1 and COL3A1 are targets of miR-29b-3p in mouse embryonic liver fibroblasts (31). In addition, the miR-29b-3p mimic decreased HSC viability, whereas the inhibitor increased it (Fig. 1E). Immunofluorescence staining results also revealed that the expression levels of α-SMA and COL1A1 were downregulated by the miR-29b-3p mimic but were upregulated by the inhibitor (Fig. 1F). Furthermore, ELISA analysis revealed that the miR-29b-3p mimic decreased the levels of IL-6, whereas the inhibitor increased these levels (Fig. 1G).

miR-29b-3p reverses HSCs activation by regulating lipid metabolism. To explore the main mechanism of miR-29b-3p in liver fibrosis, KEGG analysis of differentially expressed genes between patients with early (I, II) and late (III, IV) liver fibrosis in the GSE33258 dataset were assessed (Fig. 2A). In addition, KEGG analysis of the target genes of hsa-miR-29b-3p was performed (Fig. S1B). 'VEGF signaling pathway' and 'fatty acid metabolism' were enriched in both. Moreover, 'Apoptosis-multiple species' and 'Autophagy-animal' were also involved.

The miR-29b-3p mimic restored the lipid droplet content in activated HSCs, as determined by oil red O and Nile red staining; however, the miR-29b-3p inhibitor had no apparent effect (Fig. 2B). The TG and TC assays also confirmed that the miR-29b-3p mimic significantly increased the levels of TG and TC, whereas the miR-29b-3p inhibitor decreased these

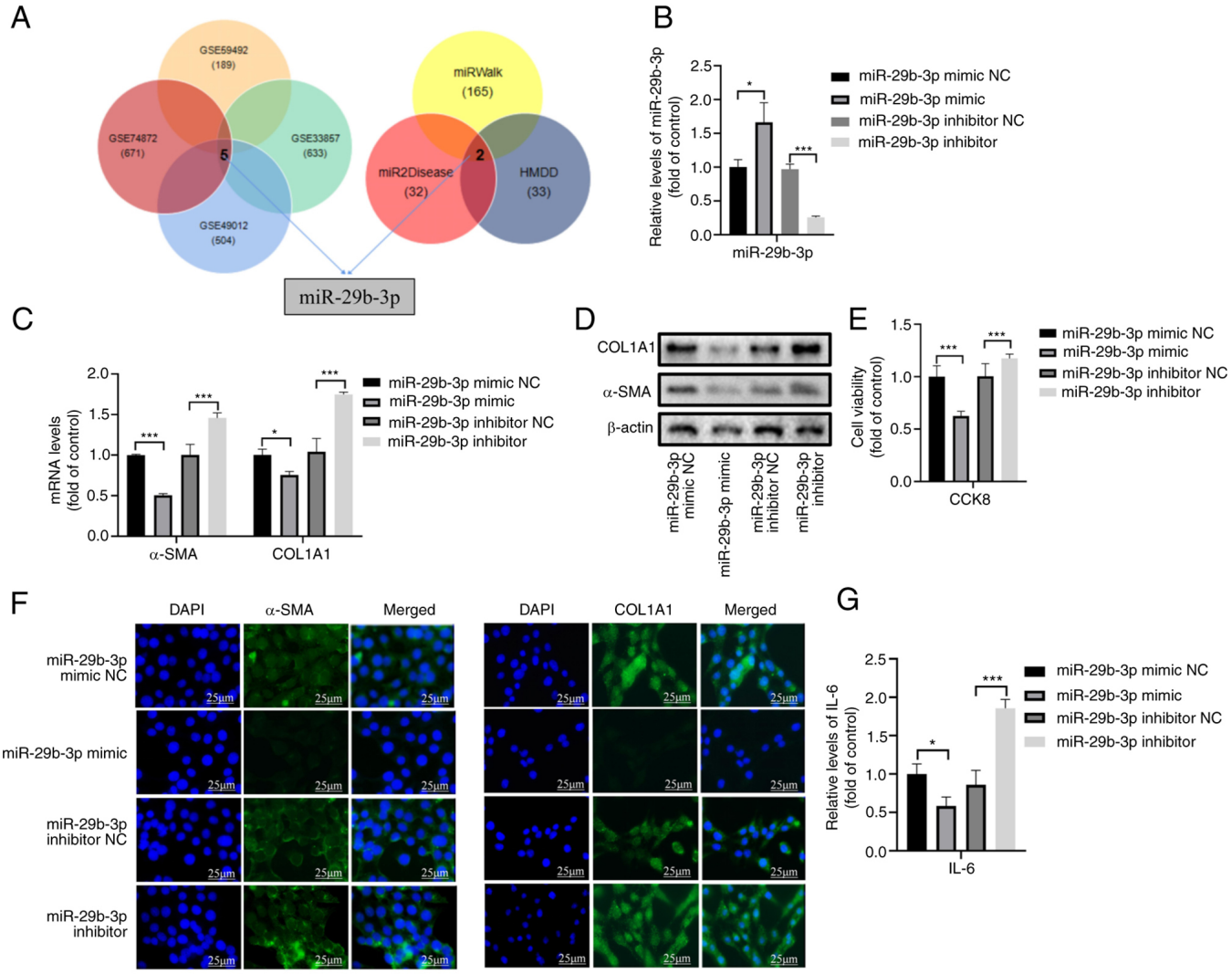

Figure 1. miR-29b-3p upregulation inhibits hepatic stellate cell development *in vitro*. (A) Screening of differentially expressed miRNAs in liver disease in the Gene Expression Omnibus database and public miRNA databases. (B) RT-qPCR analysis of miR-29b-3p in LX-2 cells transfected with miR-29b-3p mimic or inhibitor. (C) RT-qPCR of α-SMA and COL1A1 in LX-2 cells transfected with miR-29b-3p mimic or inhibitor. (D) Western blot analysis of α-SMA and COL1A1 in LX-2 cells transfected with miR-29b-3p mimic or inhibitor. (E) Viability of LX-2 cells transfected with miR-29b-3p mimic or inhibitor. (F) Immunofluorescence staining of COL1A1 and α-SMA in LX-2 cells transfected with miR-29b-3p mimic or inhibitor. (G) ELISA analysis of IL-6 in LX-2 cells. Data are expressed as the mean ± SD (n=3). *P<0.05, ***P<0.001. miR/miRNA, microRNA; NC, negative control; RT-qPCR, reverse transcription-quantitative PCR.

levels (Fig. 2C). It has previously been reported that lipoprotein lipase (LPL) and HMGCR, as key enzymes in TG and cholesterol metabolism, are target genes of miR-29b-3p (32). The present study demonstrated that the mRNA and protein expression of LPL and HMGCR were inhibited by the miR-29b-3p mimic and activated by the miR-29b-3p inhibitor (Figs. 2D, E and S1C). Notably, the results revealed that the miR-29b-3p mimic increased TC levels and inhibited the expression levels of HMGCR, which is a rate-limiting enzyme of cholesterol synthesis.

miR-29b-3p inhibits the proliferation of activated HSCs through the VEGF pathway. Although lipid droplets were partially recovered in cells transfected with the miR-29b-3p mimic, trypan blue staining revealed that the miR-29b-3p mimic induced cell death (Fig. 3A). As shown in Figs. 2A and S1, the VEGF pathway may serve an important role in the development of liver fibrosis.

The VEGF family has four members: VEGFA, VEGFB, VEGFC and VEGFD. Except for VEGFC, the mRNA expression levels of other VEGF genes were inhibited by the miR-29b-3p mimic and activated by the miR-29b-3p inhibitor (Fig. 3B). VEGFA had the highest expression among them (33). In addition, VEGFA was predicted to be a target of miR-29b-3p through TargetScan, miRDB and miRWalk analyses (Fig. S2A). The miR-29b-3p mimic decreased the protein expression levels of VEGFA, whereas the miR-29b-3p inhibitor had the opposite effect (Figs. 3C and S2B). Immunofluorescence assays revealed that the miR-29b-3p mimic downregulated the expression levels of VEGFA, whereas the inhibitor upregulated them (Fig. 3D). Notably, VEGFA was confirmed as a direct target gene of miR-29b-3p via the luciferase assay (Fig. 3E).

The present study further verified the function of the miR-29b-3p/VEGFA axis. RT-qPCR confirmed successful transfection of the cells with the VEGFA siRNA (Fig. S2C).

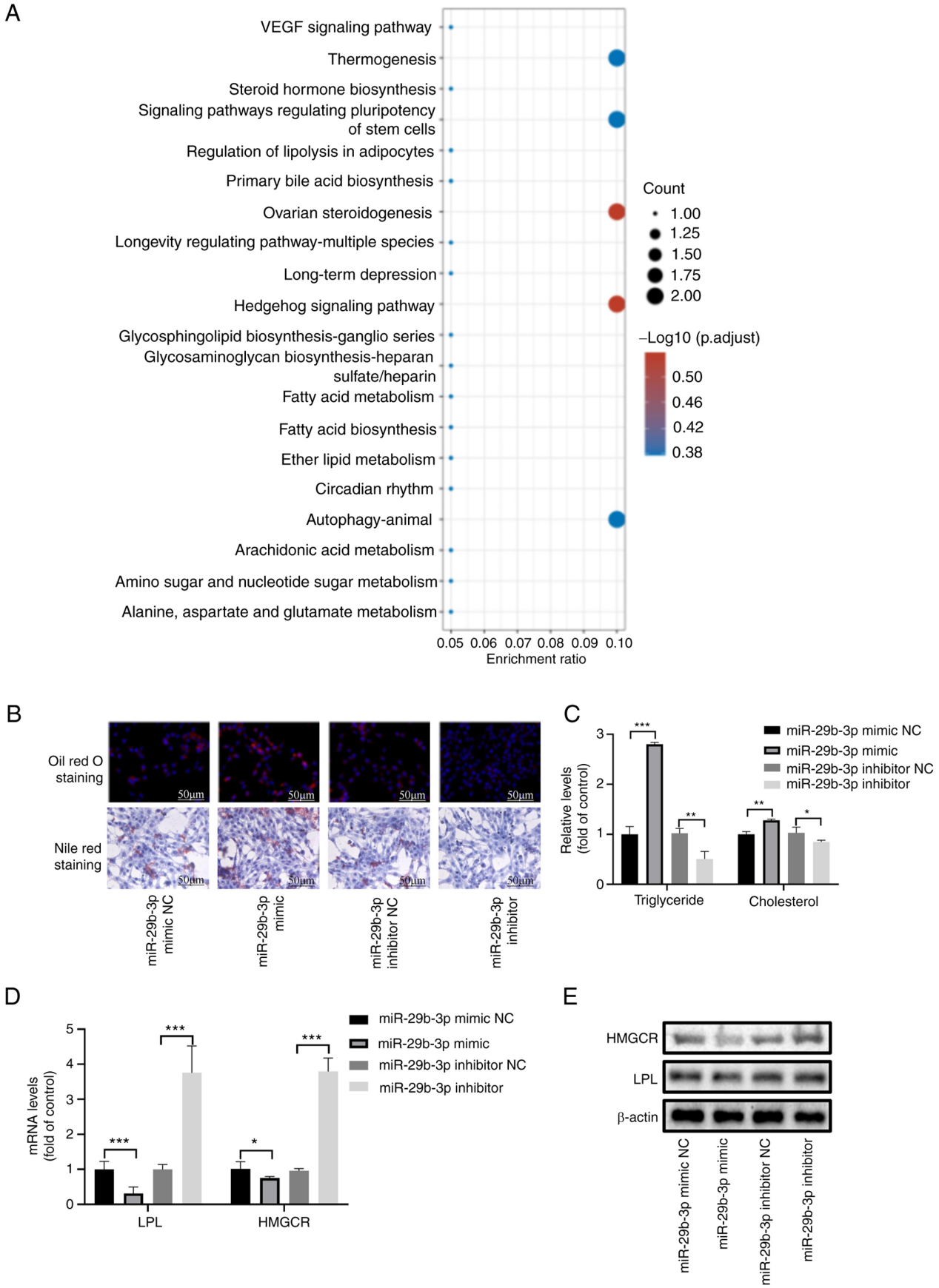

Figure 2. miR-29b-3p reverses hepatic stellate cell activation by regulating lipid metabolism. (A) Kyoto Encyclopedia of Genes and Genomes enrichment of differentially expressed genes between patients with early liver fibrosis (stages I and II) and those with late liver fibrosis (stages III and IV). (B) Nile red staining and oil red O staining of lipid droplets in LX-2 cells transfected with miR-29b-3p mimic or inhibitor. (C) Detection of triglyceride and cholesterol levels in LX-2 cells transfected with miR-29b-3p mimic or inhibitor. (D) Reverse transcription-quantitative PCR of LPL and HMGCR in LX-2 cells transfected with miR-29b-3p mimic or inhibitor. (E) Western blot analysis of LPL and HMGCR in LX-2 cells transfected with miR-29b-3p mimic or inhibitor. Data are expressed as the mean ± SD (n=3). *P<0.05, **P<0.01, ***P<0.001. LPL, lipoprotein lipase; miR/miRNA, microRNA; NC, negative control.

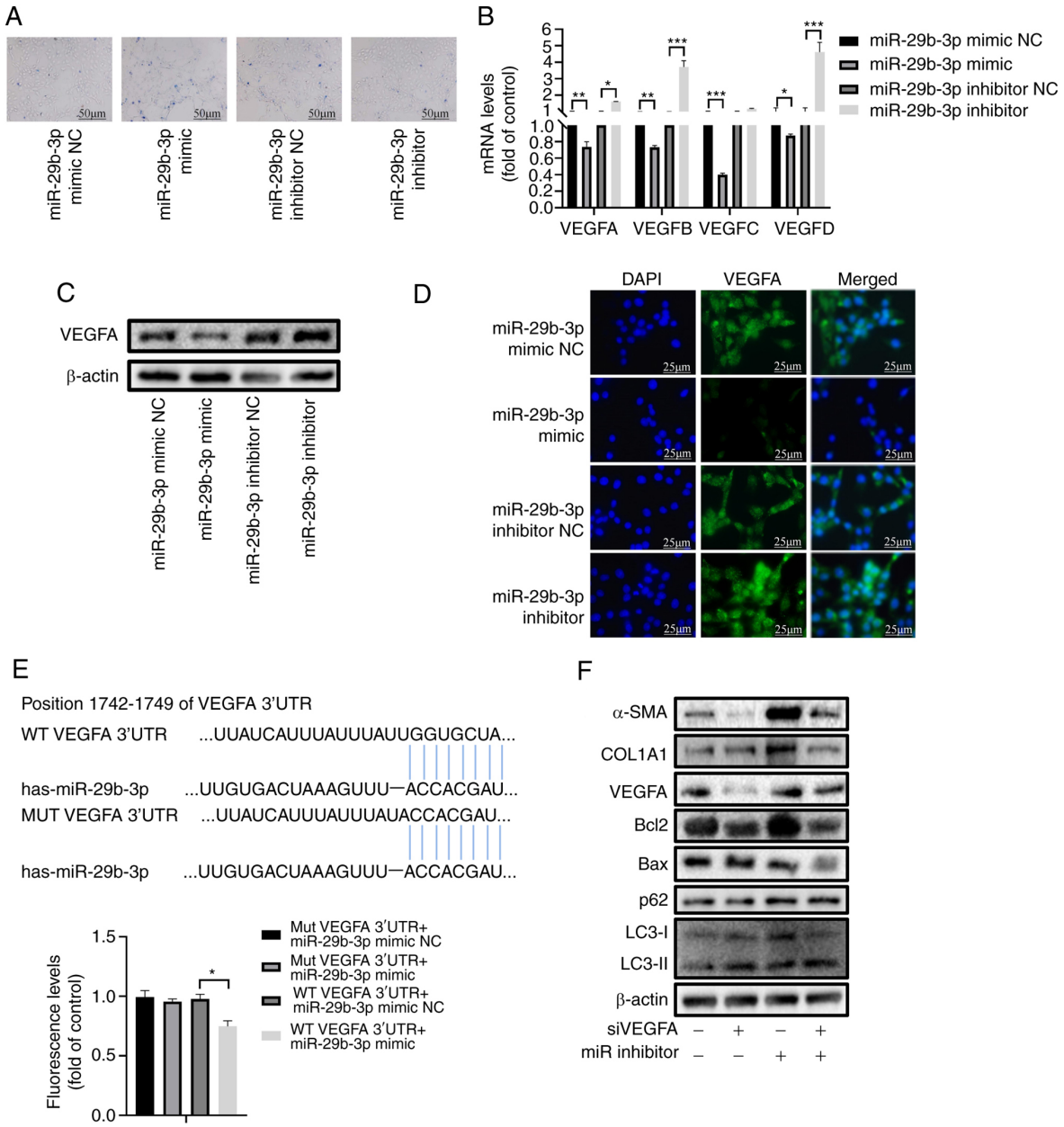

Figure 3. miR-29b-3p inhibits the proliferation of activated hepatic stellate cells through the VEGF pathway. (A) Trypan blue staining of LX-2 cells transfected with miR-29b-3p mimic or inhibitor. (B) Reverse transcription-quantitative PCR analysis of VEGFA, VEGFB, VEGFC and VEGFD. (C) Western blot analysis of VEGFA, in LX-2 cells transfected with miR-29b-3p mimic or inhibitor. (D) Immunofluorescence staining of VEGFA in LX-2 cells transfected with miR-29b-3p mimic or inhibitor. (E) Luciferase assay testing VEGFA binding with miR-29b-3p. (F) Western blot analysis of α-SMA, COL1A1, VEGFA, Bax/Bcl-2, p62 and LC3-II/ LC3-I in LX-2 cells transfected with miR-29b-3p mimic or inhibitor. Data are expressed as the mean ± SD (n=3). *P<0.05, **P<0.01, ***P<0.001. LPL, lipoprotein lipase; miR/miRNA, microRNA; MUT, mutant; NC, negative control; WT, wild-type.

Compared with in the control group, VEGFA siRNA inhibited the protein expression levels of the fibrotic biomarkers COL1A1 and α-SMA, whereas the miR-29b-3p inhibitor increased the expression levels of these proteins. In addition, VEGFA siRNA increased the expression levels of Bax/Bcl-2 and LC3-II/LC3-I while decreasing p62, whereas the miR-29b-3p inhibitor had the opposite effects (Figs. 3F and S2D).

VEGFR1 and VEGFR2 serve different roles in HSC activation. VEGFA has two main receptors: VEGFR1 and VEGFR2. RT-qPCR and western blot analysis demonstrated that VEGFR1 and VEGFR2 siRNAs were successfully transfected into LX-2 cells (Fig. S3A-C). Wound healing and adhesion assays demonstrated that VEGFR2 knockdown significantly inhibited the migratory and adhesive ability of LX-2 cells, whereas VEGFR1 knockdown had little effect (Fig. 4A and B). In addition, Annexin V-FITC/PI double staining and ELISA showed that VEGFR1 and VEGFR2 knockdown both induced the apoptosis and inhibited the inflammatory reaction via decreasing IL-6 expression of LX-2 cells (Fig. 4C and D).

Notably, western blot analysis was performed to detect the expression levels of autophagy-related proteins and it was revealed that VEGFR1 knockdown inhibited the expression levels of LC3-II/LC3-I and increased the expression levels of p62 in activated HSCs, whereas VEGFR2 knockdown increased the expression levels of LC3-II/LC3-I and inhibited the

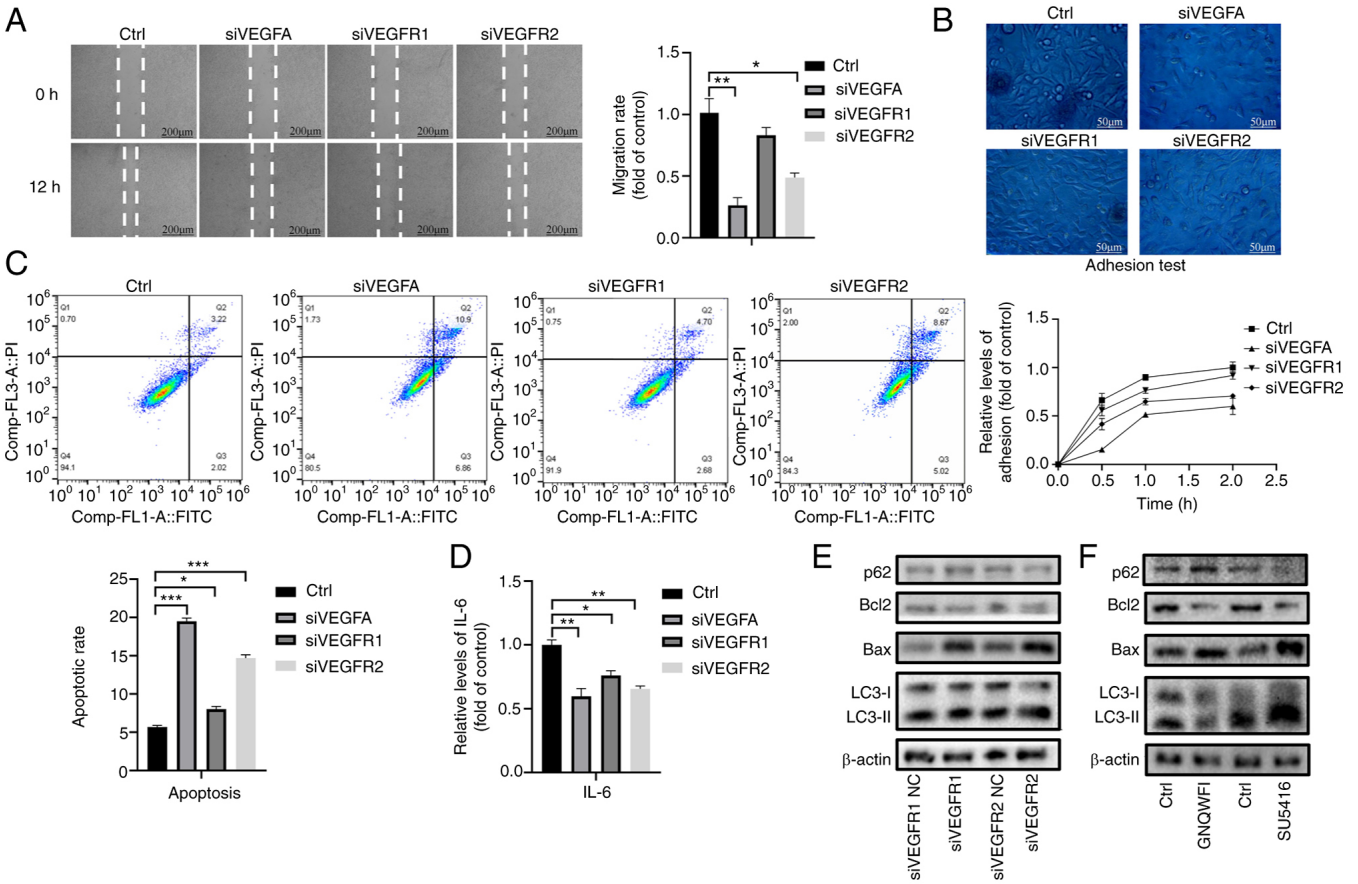

Figure 4. VEGFR1 and VEGFR2 have different roles in hepatic stellate cell activation. (A) Wound healing assay of LX-2 cells transfected with VEGFA siRNA, VEGFR1 siRNA and VEGR2 siRNA. (B) Adhesion assay of LX-2 cells transfected with VEGFA siRNA, VEGFR1 siRNA and VEGR2 siRNA. (C) Annexin V-FITC/PI double staining of LX-2 cells transfected with VEGFA siRNA, VEGFR1 siRNA and VEGR2 siRNA. (D) ELISA analysis of IL-6 in LX-2 cells transfected with VEGFA siRNA, VEGFR1 siRNA and VEGR2 siRNA. (E) Western blot analysis of Bax/Bcl-2, p62 and LC3-II/ LC3-I in LX-2 cells transfected with VEGFR1 siRNA and VEGFR2 siRNA. (F) Western blot analysis of Bax/Bcl-2, p62 and LC3-I/LC3-II in LX-2 cells treated with GNQWFI and SU5416. Data are expressed as the mean ± SD (n=3). *P<0.05, **P<0.01, ***P<0.001. siRNA/si, small interfering RNA.

expression levels of p62 in activated HSCs (Figs. 4E and S3D). LX-2 cells were further treated with the VEGFR1-specific inhibitor GNQWFI and the VEGFR2-specific inhibitor SU5416 at concentrations of 0.02, 0.2, 2 and 10 μM (Fig. S3E). The results revealed that 2 μM GNQWFI and 0.2 μM SU5416 significantly inhibited the expression levels of VEGFR1 and VEGFR2, respectively (Fig. S3C). Western blot analysis demonstrated that the autophagy-related protein LC3-II/LC3-I was decreased after GNQWFI treatment but increased after SU5416 treatment (Figs. 4F and S3F). In addition, both knockdown of VEGFR1 and VEGFR2 increased the expression levels of Bax/Bcl-2 (Figs. 4E, F and S3D).

VEGFR2 knockdown induces autophagy via PI3K/AKT/mTOR/ULK1, promotes ubiquitination of HSP60 and induces protein degradation. Numerous studies have reported that the PI3K/AKT pathway is the main downstream signal of VEGFR2 and is essential in inducing autophagy (17,34,35). Western blot analysis revealed that VEGFR2 siRNA significantly reduced the phosphorylation levels of PI3K and AKT, and these changes were reversed by the PI3K-specific agonist 740Y-P (Figs. 5A and S4A). Western blot analysis also revealed that VEGFR2 knockdown inhibited the phosphorylation of mTOR and ULK1, whereas 740Y-P had the opposite effect (Fig. 5A).

In addition to inducing autophagy, VEGFR2 knockdown simultaneously promoted cell apoptosis (Fig. 4C). Analysis using GeneMania, a protein interaction prediction website, revealed a potential interaction between VEGFR2 and the mitochondrial stabilizing protein HSP60 (Fig. S4B). A fluorescence colocalization assay revealed that VEGFR2 and HSP60 were colocalized in the LX-2 cytoplasm under normal conditions, and the colocalization level was markedly weakened after transfection with VEGFR2 siRNA (Fig. 5B). Immunoprecipitation assays showed that the VEGFR2 protein could bind to the HSP60 protein (Fig. 5C). RT-qPCR and western blot analysis revealed that the CMV-14-HSP60 plasmid was successfully transfected into LX-2 cells (Figs. S4C, 4D and 5D). Western blot analysis also revealed that the expression levels of AIF, cytochrome *c* and cleaved caspase-9/pro-caspase-9 were markedly increased after VEGFR2 knockdown; these effects were reversed by HSP60 overexpression (Figs. 5D and S4D). VEGFR2 knockdown also induced an imbalance in mitochondrial membrane potential, but HSP60 overexpression reversed this imbalance (Fig. 5E).

The present results revealed that VEGFR2 knockdown decreased the protein expression levels of HSP60, whereas the miR-29b-3p inhibitor reversed this condition (Fig. 5F).

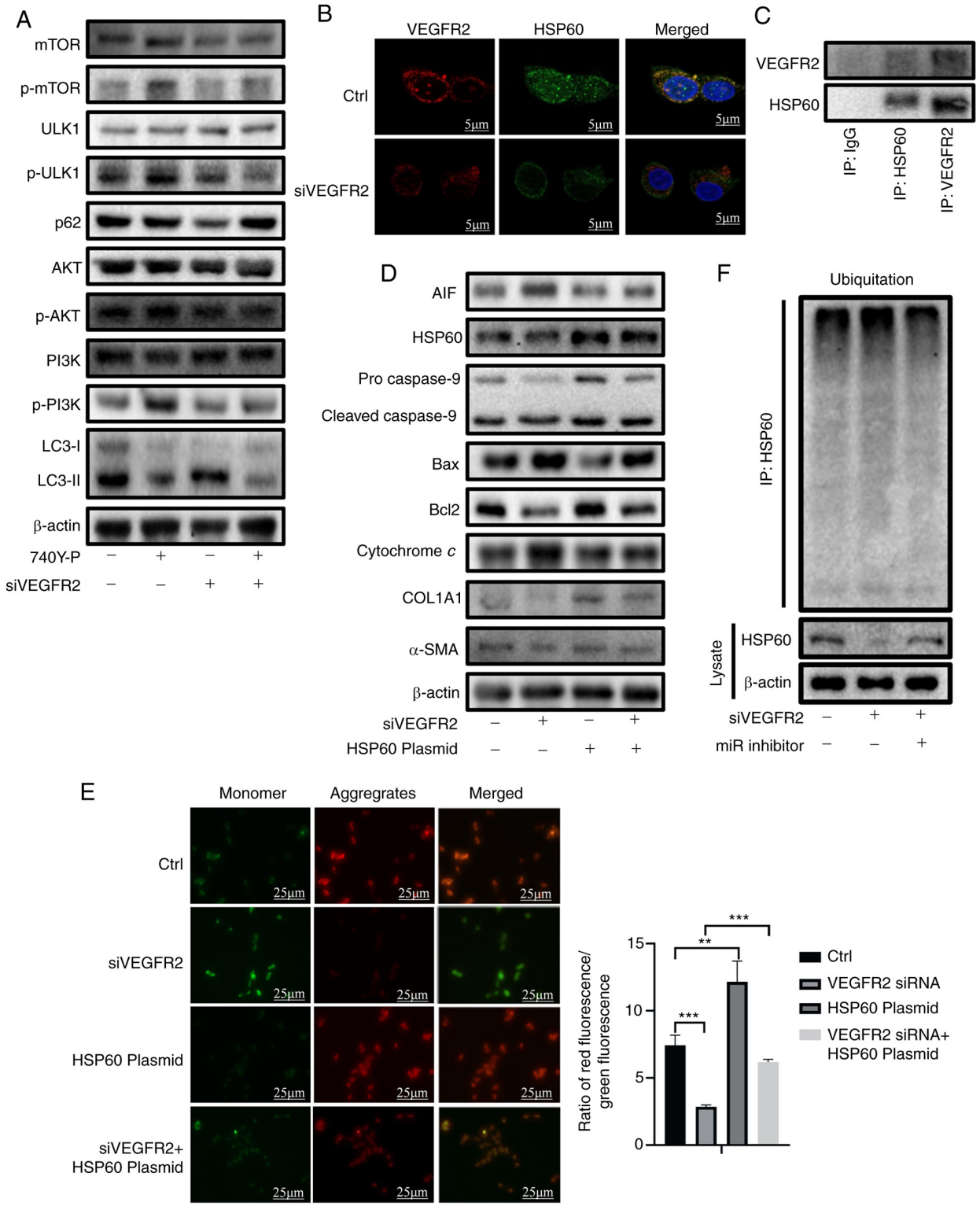

Figure 5. VEGFR2 knockdown induces autophagy via the PI3K/AKT/mTOR/ULK1 axis and induces apoptosis by promoting ubiquitination of HSP60. (A) Western blot analysis of PI3K, p-PI3K, AKT, p-AKT, mTOR, p-mTOR, ULK1, p-ULK1, p62 and LC3-II/LC3-I in LX-2 cells transfected with VEGFR2 siRNA and treated with 740Y-P. (B) Colocalization of VEGFR2 and HSP60 as determined by immunofluorescence. (C) Immunoprecipitation analysis of VEGFR2 and HSP60 in LX-2 cells. (D) Western blot analysis of α-SMA, COL1A1, AIF, HSP60, cleaved caspase-9/pro-caspase-9, Bax/Bcl-2 and cytochrome *c* in LX-2 cells transfected with VEGFR2 siRNA and HSP60 plasmid. (E) JC-1 assay of LX-2 cells transfected with VEGFR2 siRNA and HSP60 plasmid. Data are expressed as the mean ± SD (n=3). (F) Western blot analysis of ubiquitination of HSP60 in LX-2 cells transfected with VEGFR2 siRNA and miR-29b-3p inhibitor. **P<0.01, ***P<0.001. HSP60, heat shock protein 60; miR, microRNA; p-, phosphorylated; siRNA/si, small interfering RNA.

Immunoprecipitation assays showed that the ubiquitination of HSP60 increased after VEGFR2 knockdown, and miR-29b-3p intervention partly reduced this increase (Figs. 5F and S4E). These findings indicated that VEGFR2 may inhibit apoptosis by binding with HSP60 to prevent its ubiquitination and degradation, and mitochondrial homeostasis (36,37).

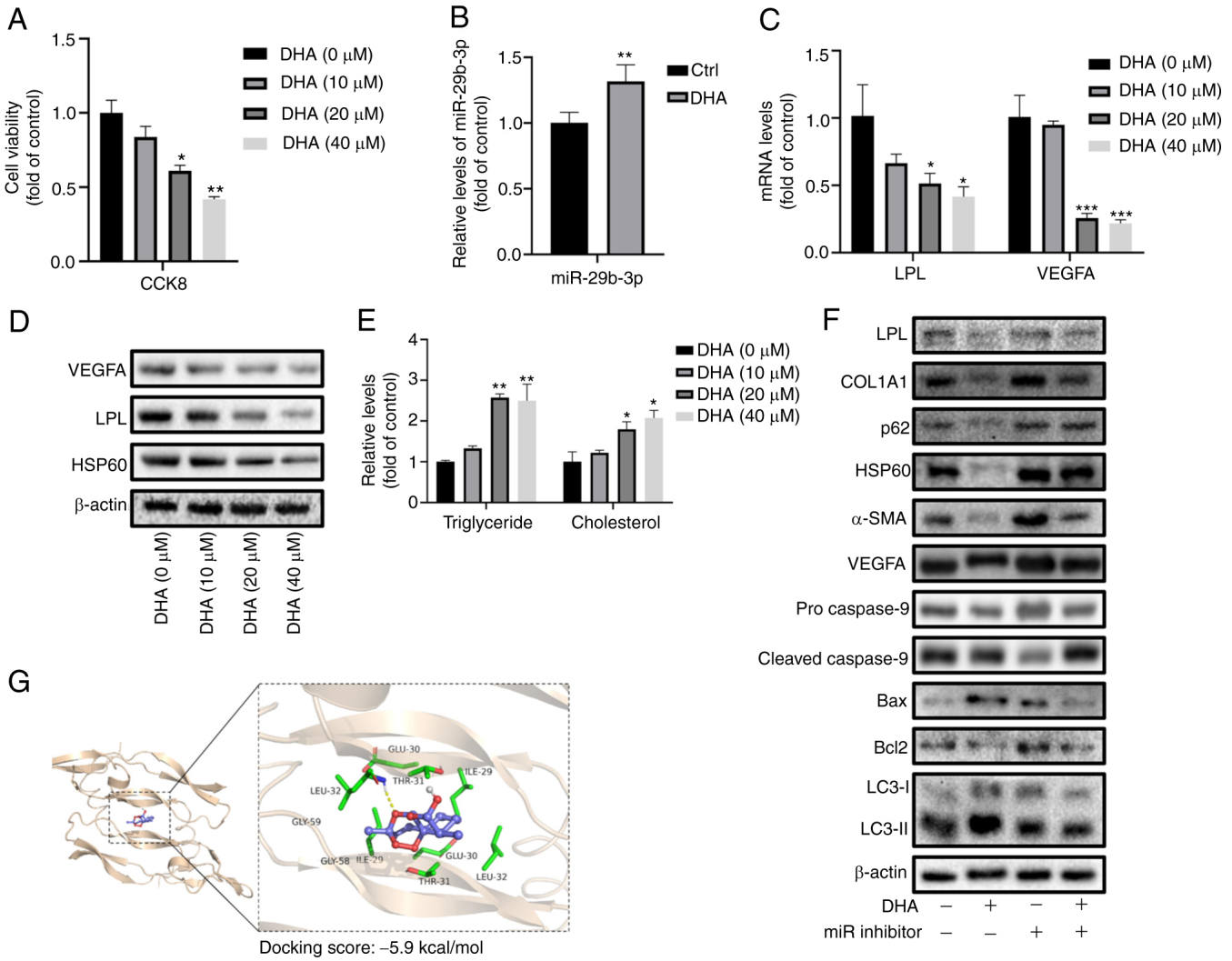

Figure 6. DHA prevents liver fibrosis by increasing the expression of miR-29b-3p. (A) Viability of LX-2 cells treated with DHA at different concentrations. *P<0.05, **P<0.01 vs. 0 μM DHA. (B) RT-qPCR analysis of miR-29b-3p in LX-2 cells treated with DHA. **P<0.01 vs. Ctrl. (C) RT-qPCR analysis of LPL and VEGFA in LX-2 cells treated with DHA at different concentrations. (D) Western blot analysis of LPL, VEGFA and HSP60 in LX-2 cells treated with DHA at different concentrations. (E) Detection of triglyceride and cholesterol levels in LX-2 cells treated with DHA at different concentrations. *P<0.05, **P<0.01, ***P<0.001 vs. 0 μM DHA. (F) Western blot analysis of Bax/Bcl-2, Beclin-1, LC3-II/ LC3-I, cleaved caspase-9/pro-caspase-9, VEGFA, α-SMA and COL1A1 in LX-2 cells treated with DHA and transfected with miR-29b-3p inhibitor. (G) Prediction of interaction between DHA and VEGFA protein via micro thermal surge instrument. Data are expressed as the mean ± SD (n=3). DHA, dihydroartemisinin; LPL, lipoprotein lipase; miR, microRNA; RT-qPCR, reverse transcription-quantitative PCR.

DHA prevents liver fibrosis by increasing the expression of miR-29b-3p. A previous study screened the small molecule agonist DHA from natural products and revealed that it could prevent fibrosis; therefore, the present study aimed to confirm the relationship between miR-29b-3p and DHA in fibrosis treatment (30).

The CCK-8 assay showed that DHA decreased the viability of LX-2 cells in a dose-dependent manner (Fig. 6A). Furthermore, miR-29b-3p expression was significantly higher in HSCs treated with DHA compared with that in the control group (Fig. 6B). The mRNA and protein expression levels of LPL and VEGFA in HSCs were significantly decreased following treatment with DHA in a dose-dependent manner (Figs. 6C, D and S5A). DHA also increased intracellular TG and TC levels (Fig. 6E), and inhibited HSP60 protein expression (Fig. 6D) in a dose-dependent manner.

Furthermore, DHA treatment enhanced the protein expression levels of Bax/Bcl-2, LC3-II/LC3-I and cleaved caspase-9/pro-caspase-9, and decreased the expression levels of p62, VEGFA, α-SMA and COL1A1 in LX-2 cells, whereas miR-29b-3p inhibition reversed these effects (Figs. 6F and S5B). In addition, molecular docking indicated a strong direct interaction of DHA with VEGFA protein (docking score, -5.9 kcal/mol), thus indicating that DHA not only regulated VEGFA mRNA via miR-29b-3p but also by directly acting on the VEGFA protein (Fig. 6G).

DHA treatment prevents liver fibrosis and hepatic injury in CCl_4-treated rats via miR-29b-3p. To further confirm the specific mechanism underlying the effects of DHA treatment on liver fibrosis, a rat model of liver fibrosis was established via intraperitoneal injection of CCl_4. An AAV8 miR-29b-3p mimic was used to increase miR-29b-3p expression via caudal vein

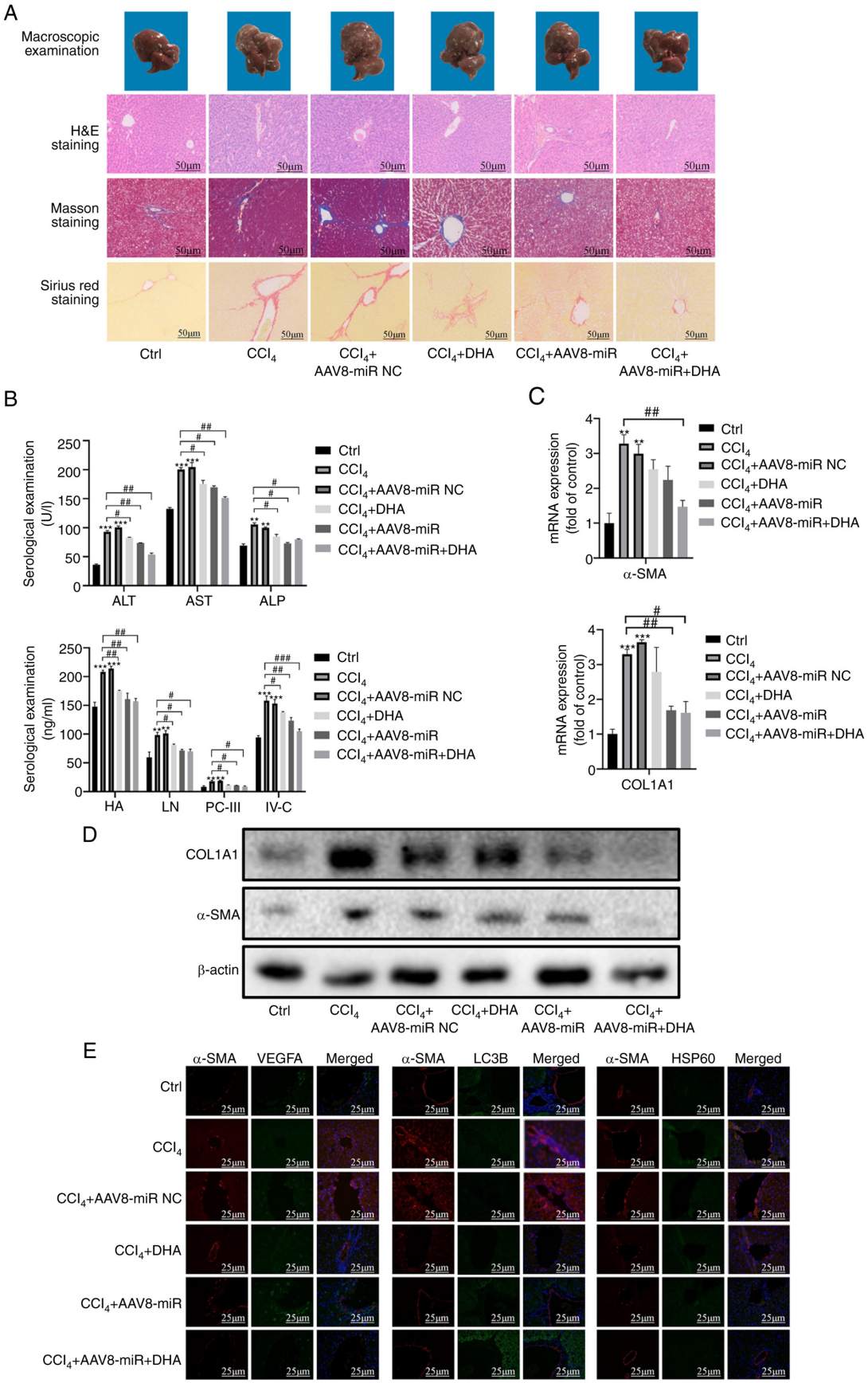

Figure 7. DHA treatment prevents liver fibrosis and hepatic injury in CCl_4-treated rats via miR-29b-3p. (A) Liver pathological changes were observed by macroscopic examination, and liver sections were stained with H&E, Masson and Sirius Red. (B) Serological examination of injury biomarkers (ALT, AST, ALP, HA111, LN, PC-III and IV-C). (C) Reverse transcription-quantitative PCR of α-SMA and COL1A1 in liver tissue. (D) Western blot analysis of α-SMA and COL1A1 in liver tissue. (E) Immunofluorescence staining of VEGFA, HSP60 and LC3 in rat liver tissue. α-SMA was used to stain hepatic stellate cells. Data are expressed as the mean ± SD (n=3). **P<0.01, ***P<0.001 vs. Ctrl; $^{\#}$P<0.05, $^{\#\#}$P<0.01 vs. CCl_4. CCl_4, carbon tetrachloride; DHA, dihydroartemisinin; H&E, hematoxylin and eosin; miR, microRNA; NC, negative control.

injection. RT-qPCR confirmed the successful intervention of AAV8 miR-29b-3p mimic in the liver of rats (Fig. S5C). Liver morphology evaluations confirmed the successful construction of the liver fibrosis model, which exhibited obvious fibrotic lesions compared with in the control group. Treatment with the miR-29b-3p mimic and DHA markedly reduced fibrotic lesions in the liver (Fig. 7A). In addition, H&E staining was used to investigate the effects of the AAV8 miR-29b-3p mimic and DHA on hepatic injury and inflammation. Intraperitoneal injection of CCl_4 induced inflammatory infiltration, hepatic fibrous septum formation and hepatocyte disorder; however, these effects were attenuated by the AAV8 miR-29b-3p mimic and DHA. The results of Masson and Sirius Red staining also revealed that large amounts of collagen and matrix were deposited around the hepatic fibrous scar area in the model group, but were effectively reduced by the AAV8 miR-29b-3p mimic and DHA (Fig. 7A). Serological examination demonstrated that hepatic injury biomarkers (ALT, AST, ALP, HA111, LN, PC-III and IV-C) were higher in the model group than in the AAV8 miR-29b-3p mimic and DHA treatment groups, which is consistent with our previous conclusion that miR-29b-3p and DHA inhibited HSC activity and reversed activated HSCs into a static condition (Fig. 7B).

The mRNA and protein expression levels of α-SMA and COL1A1 were significantly upregulated in the model group, whereas they were downregulated by the AAV8 miR-29b-3p mimic and DHA (Figs. 7C, D and S5D). Immunofluorescence double staining revealed that the expression of VEGFA and HSP60 in fibrotic tissue was inhibited by the AAV8 miR-29b-3p mimic or DHA, whereas LC3B expression was increased. Fibrotic liver tissue was stained with α-SMA (Fig. 7E).

Discussion

The pathogenesis of liver fibrosis is complex and difficult to elucidate. Liver fibrosis is a common pathological process associated with most types of acute or chronic liver disease, which can ultimately progress to liver cirrhosis and liver cancer without timely treatment. Although the etiology of these diseases differs, they are all characterized by hepatic fibrosis, and early and long-term anti-hepatic fibrosis treatment are recommended for these conditions (38,39); however, there is still no effective method to cure liver fibrosis. Natural products have attracted great interest from researchers because of their unique chemical structures and diverse biological activity. In addition, medicinal plants have been widely used to prevent and treat various diseases. DHA is a derivative of artemisinin, which is a commonly used antimalarial drug; however, DHA has also been reported to exert anti-inflammatory, antitumor, antibacterial and antiviral activities (40,41). We previously showed that DHA could reduce CCl_4-induced liver fibrosis *in vivo*, and induce activation of HSCs aging and HSCs apoptosis *in vitro* (15,16). The present study aimed to clarify the mechanism by which DHA could inhibit HSCs activation and induce cell death via miR-29b-3p.

Increasing evidence has shown that miRNAs have an important role in cell survival and development, and great progress has been achieved in miRNA-targeted therapy. A miR-34 mimic encapsulated in lipid nanoparticles that inhibits tumor cell growth has been evaluated in phase II clinical trials (NCT01829971) (42), and locked nucleic acid therapy inhibiting miR-122 for the treatment of hepatitis has also entered clinical trials (43,44). The present results were consistent with the prediction that miR-29b-3p has a key role in recovering HSC lipid droplets and inducing cell death. Moreover, we aim to collect liver samples from patients with liver fibrosis of different stages, and to further compare the differential expression of miR-29b-3p in a future study.

The main components of lipid droplets are retinol, TG and cholesterol. Lipid droplet loss can induce static HSCs activation. In the present study, miR-29b-3p promoted TG and TC levels in HSCs, and reversed HSC activation. LPL is the rate-limiting enzyme for the degradation of TGs into glycerol and free fatty acids. Due to the special cell structure of lipid droplets in HSCs, LPL may have an important role in metabolism of lipid droplets. Previous studies have reported a strong correlation between LPL and HSCs activation and liver fibrosis (45,46). The present study verified the hypothesis that miR-29b-3p may participate in intracellular lipid metabolism by regulating LPL and HMGCR via western blot analysis and RT-qPCR analysis. The results revealed that LPL was regulated by miR-29b-3p and influenced by DHA in a dose-dependent manner. LPL regulates lipid metabolism and maintains an energy balance, and is primarily located on the capillary endothelial cell surface. A previous study reported that LPL was enhanced in HSCs, not hepatocytes, in a model of nonalcoholic fatty liver disease (6). Enhanced LPL has been reported to induce the accumulation of free cholesterol and to decrease TG levels in HSCs via TLR4- and Bambi-related signals, increasing the susceptibility of HSCs to TGF-β-induced HSC activation. The present study also confirmed that LPL inhibition in HSCs contributed to the increase in TGs and recovery of lipid droplets; with the decrease in LPL expression level detected following intervention with the miR-29b-3p mimic, TG began to accumulate in HSCs and lipid droplets gradually recovered. However, the decrease in HMGCR conflicts with the increase in cholesterol; HMGCR is a key enzyme in the cholesterol synthesis pathway. Generally, increased HMGCR could can induce the synthesis of cholesterol. Kurtz *et al* (32) reported a similar phenomenon. This previous study found that among the genes upregulated by miR-29b-3p, the anti-lipogenic deacetylase SIRT1 and aryl hydrocarbon receptor exhibited the greatest differences. These two genes may reverse the effect of HMGCR on cholesterol. Moreover, other cholesterol enzymes, such as lecithin-cholesterol acyltransferase and acyl-coenzyme A-cholesterol acyltransferase, may also contribute to cholesterol upregulation. It was hypothesized that this may explain the contradictory phenomenon that HMGCR expression was decreased whereas cholesterol was increased after miR-29b-3p mimic intervention.

Previous studies have shown that VEGF signaling in sinusoidal endothelial cells negatively influences liver fibrosis development (47,48). The present study aimed to explore the function of the VEGF pathway in HSCs. VEGFA was identified as a direct target of miR-29b-3p, which simultaneously regulated multiple functions of HSCs, including adhesion, migration, survival and the inflammatory response. Notably, VEGFR1 and VEGFR2, as receptors of VEGFA, had different roles. Although knockdown of both inhibited fibrosis, and caused apoptosis and inhibited inflammation, VEGFR1

knockdown had no significant effect on cell migration and adhesion. By contrast, VEGFR2 knockdown significantly inhibited cell migration and adhesion. Notably, autophagy was decreased after VEGFR1 silencing but was increased after VEGFR2 silencing. It was hypothesized that VEGFR1 and VEGFR2 competitively bind to VEGFA, and that VEGFR2 plays a greater role after VEGFR1 silencing and protects cells from autophagy. By contrast, when VEGFR2 was silenced, autophagy was increased. It has previously been suggested that VEGFR2 is the main receptor of VEGF, whereas VEGFR1 is considered a decoy receptor that weakens the binding between VEGFA and VEGFR2 (48). A previous study reported that the ULK1 complex may act as a bridge connecting the upstream trophic receptor mTOR or the energy receptor AMPK and downstream autophagy *in vivo* (15). Notably, p-mTOR can phosphorylate ULK1 to disrupt the binding between ATG3 and ULK1, thus destabilizing it and ultimately inhibiting the initiation of autophagy (34,35). In the present study, it was revealed that VEGFA/VEGFR2 regulated autophagy via the PI3K/AKT/mTOR/ULK1 pathway. It was hypothesized that when VEGFR1 was silenced, VEGFR2 worked more and inhibited HSCs autophagy, whereas when VEGFR2 was silenced, the autophagy of HSCs was activated. However, autophagy is a complex cellular event involving multigene regulation. The present study only preliminarily explored the function of two VEGFRs through siRNA and specific inhibitors. At present, the dynamic process of autophagy over time is not clear and further research is required (15,35,37).

To the best of our knowledge, the present study is the first to show that HSP60 is an intermediate protein in DHA-induced mitochondrial apoptosis, and its ubiquitination and degradation may be a key event leading to the imbalance of mitochondrial homeostasis after VEGFR2 silencing. It has previously been reported that after VEGF intervention, phosphorylation and ubiquitination of zonula cluster-1 occur, further influencing vascular permeability (36). ATP7A has been identified as an interacting protein of VEGFR2 that assists VEGFR2 entry into the cytoplasm. Where ATP7 is ubiquitinated, autophagy is induced (37). In recent years, epigenetics has emerged as an important research topic. An increasing number of studies have shown that several epigenetic modifications, such as methylation, acetylation and ubiquitination, participate in cell survival. Furthermore, HSP60 has been reported to be important in liver disease. Yang *et al* reported that the expression of HSP60 was significantly upregulated in the liver tissue of mice with liver fibrosis and that this upregulation was reversed by a miR-29a mimic (49). Mazo *et al* also revealed that the expression of HSP60 mRNA was significantly increased in a rat model of nonalcoholic steatohepatitis, whereas S-nitroso-N-acetylcysteine decreased the expression of HSP60 and COL1A1 and alleviated liver fibrosis (50). HSP60 is mainly involved in protein transport and folding under physiological conditions. When the cell is injured, HSP60 acts as a stress protein to resist various damaging effects. In addition, HSP60 can repair mitochondrial cytochrome *c* in combination with HSP10, and can protect mitochondria (51). HSP60 overexpression has been reported to increase the expression levels of the Bcl-XL gene and reduce the expression of Bax, stabilizing mitochondrial membrane potential and inhibiting activation of the caspase-9-related pathway (52). The HSP60 amino acid sequence contains numerous potential phosphorylation sites and other post-translational modifications (PTMs), such as ubiquitination, oxidation, S-nitrosylation and acetylation, can also occur in HSP60 protein. PTMs are essential for maintaining HSP60 function in a number of processes, such as mitochondrial dysfunction, tumor invasiveness, and delay or facilitation of apoptosis (53). The present study revealed that VEGFR2 could protect HSP60 from ubiquitination and degradation.

Notably, VEGFR2 may also be involved in the ubiquitination of several autophagy genes. The present study only examined the mechanism by which VEGFR2 regulates autophagy through the classical PI3K/AKT signaling pathway; however, the differences in autophagy activity may be the result of a variety of epigenetic modifications. Therefore, it is important to further explore the interactions among chaperone proteins, VEGFR2, apoptosis and autophagy, especially the regulatory crosstalk between different epigenetic modifications.

There are some limitations in the present study. Firstly, the LX-2 cell line was selected as the research subject, whereas primary HSCs were not assessed. Secondly, this study did not verify the correlation between HSP60, the PI3K/AKT pathway and the miR-29b-3p/VEGFA axis. Thirdly, despite post-transcriptional interactions between VEGFR2 and HSP60 proteins being detected in LX-2 cells, protein-mRNA interactions during transcription may also play key roles.

In conclusion, DHA may inhibit the activation of HSCs and induce the programmed death of HSCs via the miR-29b-3p/VEGFA axis. Furthermore, VEGFR2 was revealed to be important in regulating autophagy and apoptosis via the PI3K/AKT/mTOR/ULK1 pathway, and by binding to HSP60 to prevent its ubiquitination and degradation (Fig. S6). The present study provided a new perspective and target for drug development in the treatment of liver fibrosis.

Acknowledgements

Not applicable.

Funding

This work was supported in part by the Natural Science Foundation of Nanjing University of Traditional Chinese Medicine (grant no. XZR2020072), Graduate Research and Innovation Projects of Jiangsu Province (grant no. KYCX21_1637) and Graduate Research and Innovation Projects of Jiangsu Province (grant no. KYCX21_1732).

Availability of data and materials

The datasets used and/or analyzed during the current study are available from the corresponding author on reasonable request.

Authors' contributions

SH, SZ and GY contributed to the conception of the study. SH, SMS and GY contributed to the funding acquisition. SH, YZ and GY performed the experiments. SH and SMS contributed to data collection and systematic analysis. SLS

contributed to the ethics approval application and animal experiments. SH, JD and YJ contributed to the design of methodology and use of software. GZ and YZ contributed to analysis and manuscript preparation. SH, YJ and GY provided resources, supervised the study and wrote the original draft. SH and GY confirm the authenticity of all the raw data. All authors read and approved the final manuscript.

Ethics approval and consent to participate

The authors confirm that all methods were carried out in accordance with the relevant guidelines and regulations. The study protocol and animal experiments were approved by the Institutional and Local Committee of Nanjing University of Chinese Medicine (approval no. A20402).

Patient consent for publication

Not applicable.

Competing interests

The authors declare that they have no competing interests.

References

1. Kisseleva T and Brenner D: Molecular and cellular mechanisms of liver fibrosis and its regression. Nat Rev Gastroenterol Hepatol 18: 151-166, 2021.
2. Hernandez-Gea V and Friedman SL: Pathogenesis of liver fibrosis. Annu Rev Pathol 6: 425-456, 2011.
3. Parola M and Pinzani M: Liver fibrosis: Pathophysiology, pathogenetic targets and clinical issues. Mol Aspects Med 65: 37-55, 2019.
4. Kang N, Gores GJ and Shah VH: Hepatic stellate cells: Partners in crime for liver metastases? Hepatology 54: 707-713, 2011.
5. Trivedi P, Wang S and Friedman SL: The power of plasticity-metabolic regulation of hepatic stellate cells. Cell Metab 33: 242-257, 2021.
6. Rupaimoole R and Slack FJ: MicroRNA therapeutics: Towards a new era for the management of cancer and other diseases. Nat Rev Drug Discov 16: 203-222, 2017.
7. Krol J, Loedige I and Filipowicz W: The widespread regulation of microRNA biogenesis, function and decay. Nat Rev Genet 11: 597-610, 2010.
8. Dong H, Lei J, Ding L, Wen Y, Ju H and Zhang X: MicroRNA: Function, detection, and bioanalysis. Chem Rev 113: 6207-6233, 2013.
9. Kim VN: MicroRNA biogenesis: Coordinated cropping and dicing. Nat Rev Mol Cell Biol 6: 376-385, 2005.
10. Su T, Xiao Y, Xiao Y, Guo Q, Li C, Huang Y, Deng Q, Wen J, Zhou F and Luo XH: Bone marrow mesenchymal stem cells-derived exosomal MiR-29b-3p regulates aging-associated insulin resistance. ACS Nano 13: 2450-2462, 2019.
11. Xue Y, Fan X, Yang R, Jiao Y and Li Y: miR-29b-3p inhibits post-infarct cardiac fibrosis by targeting FOS. Biosci Rep 40: BSR20201227, 2020.
12. Novo E, Cannito S, Zamara E, Valfrè di Bonzo L, Caligiuri A, Cravanzola C, Compagnone A, Colombatto S, Marra F, Pinzani M and Parola M: Proangiogenic cytokines as hypoxia-dependent factors stimulating migration of human hepatic stellate cells. Am J Pathol 170: 1942-1953, 2007.
13. Sun J, Shi L, Xiao T, Xue J, Li J, Wang P, Wu L, Dai X, Ni X and Liu Q: microRNA-21, via the HIF-1α/VEGF signaling pathway, is involved in arsenite-induced hepatic fibrosis through aberrant cross-talk of hepatocytes and hepatic stellate cells. Chemosphere 266: 129177, 2021.
14. Huang YH and Yeh CT: Functional Compartmentalization of HSP60-Survivin interaction between mitochondria and cytosol in cancer cells. Cells 9: 23, 2019.
15. Zhang Z, Yao Z, Zhao S, Shao J, Chen A, Zhang F and Zheng S: Interaction between autophagy and senescence is required for dihydroartemisinin to alleviate liver fibrosis. Cell Death Dis 8: e2886, 2017.
16. Chen Q, Chen L, Kong D, Shao J, Wu L and Zheng S: Dihydroartemisinin alleviates bile duct ligation-induced liver fibrosis and hepatic stellate cell activation by interfering with the PDGF-βR/ERK signaling pathway. Int Immunopharmacol 34: 250-258, 2016.
17. Chen Q, Chen L, Wu X, Zhang F, Jin H, Lu C, Shao J, Kong D, Wu L and Zheng S: Dihydroartemisinin prevents liver fibrosis in bile duct ligated rats by inducing hepatic stellate cell apoptosis through modulating the PI3K/Akt pathway. IUBMB Life 68: 220-231, 2016.
18. Seeliger D and de Groot BL: Ligand docking and binding site analysis with PyMOL and Autodock/Vina. J Comput Aided Mol Des 24: 417-422, 2010.
19. Murakami Y, Toyoda H, Tanahashi T, Tanaka J, Kumada T, Yoshioka Y, Kosaka N, Ochiya T and Taguchi YH: Comprehensive miRNA expression analysis in peripheral blood can diagnose liver disease. PLoS One 7: e48366, 2012.
20. Vuppalanchi R, Liang T, Goswami CP, Nalamasu R, Li L, Jones D, Wei R, Liu W, Sarasani V, Janga SC and Chalasani N: Relationship between differential hepatic microRNA expression and decreased hepatic cytochrome P450 3A activity in cirrhosis. PLoS One 8: e74471, 2013.
21. Blaya D, Coll M, Rodrigo-Torres D, Vila-Casadesús M, Altamirano J, Llopis M, Graupera I, Perea L, Aguilar-Bravo B, Díaz A, *et al*: Integrative microRNA profiling in alcoholic hepatitis reveals a role for microRNA-182 in liver injury and inflammation. Gut 65: 1535-1545, 2016.
22. Matsuura K, De Giorgi V, Schechterly C, Wang RY, Farci P, Tanaka Y and Alter HJ: Circulating let-7 levels in plasma and extracellular vesicles correlate with hepatic fibrosis progression in chronic hepatitis C. Hepatology 64: 732-745, 2016.
23. Zhang J, Huang J, Liu W, Ding L, Cheng D and Xiao H: Identification of common oncogenic genes and pathways both in osteosarcoma and Ewing's sarcoma using bioinformatics analysis. J Immunol Res 2022: 3655908, 2022.
24. Wang Z, Zhang J, Feng T, Zhang D, Pan Y, Liu X, Xu J, Qiao X, Cui W and Dong L: Construction of lncRNA-Mediated competing endogenous RNA networks correlated With T2 asthma. Front Genet 13: 872499, 2022.
25. Zhong T, Li Z, You ZH, Nie R and Zhao H: Predicting miRNA-disease associations based on graph random propagation network and attention network. Brief Bioinform 23: bbab589, 2022.
26. Li G, Sun J, Zhang J, Lv Y, Liu D, Zhu X, Qi L, Chen Z, Ye Z, Su X and Li L: Identification of Inflammation-related biomarkers in diabetes of the exocrine pancreas with the use of weighted gene Co-Expression network analysis. Front Endocrinol (Lausanne) 13: 839865, 2022.
27. Mostafavi S and Morris Q: Combining many interaction networks to predict gene function and analyze gene lists. Proteomics 12: 1687-1696, 2012.
28. Wang S, Shen L and Luo H: Identification and Validation of Key miRNAs and a microRNA-mRNA Regulatory Network Associated with Ulcerative Colitis. DNA Cell Biol 40: 147-156, 2021.
29. Matsuura K, De Giorgi V, Schechterly C, Wang RY, Farci P, Tanaka Y and Alter HJ: Circulating let-7 levels in plasma and extracellular vesicles correlate with hepatic fibrosis progression in chronic hepatitis C. Hepatology 64: 732-745, 2016.
30. Xia S, Wang Z, Chen L, Zhou Y, Li Y, Wang S, Chen A, Xu X, Shao J, Zhang Z, *et al*: Dihydroartemisinin regulates lipid droplet metabolism in hepatic stellate cells by inhibiting lncRNA-H19-induced AMPK signal. Biochem Pharmacol 192: 114730, 2021.
31. Cutroneo KR, White SL, Phan SH and Ehrlich HP: Therapies for bleomycin induced lung fibrosis through regulation of TGF-beta1 induced collagen gene expression. J Cell Physiol 211: 585-589, 2007.
32. Kurtz CL, Fannin EE, Toth CL, Pearson DS, Vickers KC and Sethupathy P: Inhibition of miR-29 has a significant lipid-lowering benefit through suppression of lipogenic programs in liver. Sci Rep 5: 12911, 2015.
33. Apte RS, Chen DS and Ferrara N: VEGF in signaling and disease: Beyond discovery and development. Cell 176: 1248-1264, 2019.
34. Aoki M and Fujishita T: Oncogenic Roles of the PI3K/AKT/mTOR Axis. Curr Top Microbiol Immunol 407: 153-189, 2017.

35. Song YM, Lee YH, Kim JW, Ham DS, Kang ES, Cha BS, Lee HC and Lee BW: Metformin alleviates hepatosteatosis by restoring SIRT1-mediated autophagy induction via an AMP-activated protein kinase-independent pathway. Autophagy 11: 46-59, 2015.
36. Muthusamy A, Lin CM, Shanmugam S, Lindner HM, Abcouwer SF and Antonetti DA: Ischemia-reperfusion injury induces occludin phosphorylation/ubiquitination and retinal vascular permeability in a VEGFR-2-dependent manner. J Cereb Blood Flow Metab 34: 522-531, 2014.
37. Ash D, Sudhahar V, Youn SW, Okur MN, Das A, O'Bryan JP, McMenamin M, Hou Y, Kaplan JH, Fukai T and Ushio-Fukai M: The P-type ATPase transporter ATP7A promotes angiogenesis by limiting autophagic degradation of VEGFR2. Nat Commun 12: 3091, 2021.
38. Hunt NJ, Kang SWS, Lockwood GP, Le Couteur DG and Cogger VC: Hallmarks of Aging in the Liver. Comput Struct Biotechnol J 17: 1151-1161, 2019.
39. Brenner C, Galluzzi L, Kepp O and Kroemer G: Decoding cell death signals in liver inflammation. J Hepatol 59: 583-594, 2013.
40. Efferth T: From ancient herb to modern drug: Artemisia annua and artemisinin for cancer therapy. Semin Cancer Biol 46: 65-83, 2017.
41. Li Q, Ma Q, Cheng J, Zhou X, Pu W, Zhong X and Guo X: Dihydroartemisinin as a sensitizing agent in cancer therapies. Onco Targets Ther 14: 2563-2573, 2021.
42. Hong DS, Kang YK, Borad M, Sachdev J, Ejadi S, Lim HY, Brenner AJ, Park K, Lee JL, Kim TY, *et al*: Phase 1 study of MRX34, a liposomal miR-34a mimic, in patients with advanced solid tumours. Br J Cancer 122: 1630-1637, 2020.
43. Zhang L, Liao Y and Tang L: MicroRNA-34 family: A potential tumor suppressor and therapeutic candidate in cancer. J Exp Clin Cancer Res 38: 53, 2019.
44. van Rooij E and Kauppinen S: Development of microRNA therapeutics is coming of age. EMBO Mol Med 6: 851-864, 2014.
45. Teratani T, Tomita K, Furuhashi H, Sugihara N, Higashiyama M, Nishikawa M, Irie R, Takajo T, Wada A, Horiuchi K, *et al*: Lipoprotein Lipase Up-regulation in hepatic stellate cells exacerbates liver fibrosis in nonalcoholic steatohepatitis in mice. Hepatol Commun 3: 1098-1112, 2019.
46. Duan X, Meng Q, Wang C, Liu Z, Liu Q, Sun H, Sun P, Yang X, Huo X, Peng J and Liu K: Calycosin attenuates triglyceride accumulation and hepatic fibrosis in murine model of non-alcoholic steatohepatitis via activating farnesoid X receptor. Phytomedicine 25: 83-92, 2017.
47. Hu C and Jiang X: Role of NRP-1 in VEGF-VEGFR2-Independent Tumorigenesis. Target Oncol 11: 501-505, 2016.
48. Simons M, Gordon E and Claesson-Welsh L: Mechanisms and regulation of endothelial VEGF receptor signalling. Nat Rev Mol Cell Biol 17: 611-625, 2016.
49. Yang YL, Wang FS, Lin HY and Huang YH: Exogenous therapeutics of Microrna-29a attenuates development of hepatic fibrosis in cholestatic animal model through regulation of phosphoinositide 3-Kinase p85 Alpha. Int J Mol Sci 21: 3636, 2020.
50. Mazo DF, de Oliveira MG, Pereira IV, Cogliati B, Stefano JT, de Souza GF, Rabelo F, Lima FR, Ferreira Alves VA, Carrilho FJ and de Oliveira CP: S-nitroso-N-acetylcysteine attenuates liver fibrosis in experimental nonalcoholic steatohepatitis. Drug Des Devel Ther 7: 553-563, 2013.
51. Samali A, Cai J, Zhivotovsky B, Jones DP and Orrenius S: Presence of a pre-apoptotic complex of pro-caspase-3, HSP60 and HSP10 in the mitochondrial fraction of Jurkat cells. EMBO 18: 2040-2048, 1999.
52. Caruso Bavisotto C, Alberti G, Vitale AM, Paladino L, Campanella C, Rappa F, Gorska M, Conway de Macario E, Cappello F, Macario AJL and Marino Gammazza A: HSP60 Post-translational modifications: Functional and pathological consequences. Front Mol Biosci 7: 95, 2020.
53. Macario AJ and de Macario EC: Molecular mechanisms in chaperonopathies: Clues to understanding the histopathological abnormalities and developing novel therapies. J Pathol 250: 9-18, 2020.

This work is licensed under a Creative Commons Attribution-NonCommercial-NoDerivatives 4.0 International (CC BY-NC-ND 4.0) License.